

BARYON LOADING OF AGN JETS MEDIATED BY NEUTRONS

K. TOMA, AND F. TAKAHARA

Department of Earth and Space Science, Graduate School of Science, Osaka University, Toyonaka 560-0043, Japan
 toma@vega.ess.sci.osaka-u.ac.jp

Accepted for publication in ApJ

ABSTRACT

Plasmas of geometrically thick, black hole (BH) accretion flows in active galactic nuclei (AGNs) are generally collisionless for protons, and involve magnetic field turbulence. Under such conditions a fraction of protons can be accelerated stochastically and create relativistic neutrons via nuclear collisions. These neutrons can freely escape from the accretion flow and decay into protons in dilute polar region above the rotating BH to form relativistic jets. We calculate geometric efficiencies of the neutron energy and mass injections into the polar region, and show that this process can deposit luminosity as high as $L_j \sim 2 \times 10^{-3} \dot{M} c^2$ and mass loading $\dot{M}_j \sim 6 \times 10^{-4} \dot{M}$ for the case of the BH mass $M \sim 10^8 M_\odot$, where \dot{M} is mass accretion rate. The terminal Lorentz factors of the jets are $\Gamma \sim 3$, and they may explain the AGN jets having low luminosities. For higher luminosity jets, which can be produced by additional energy inputs such as Poynting flux, the neutron decay still can be a dominant mass loading process, leading to e.g., $\Gamma \sim 50$ for $L_{j,\text{tot}} \sim 3 \times 10^{-2} \dot{M} c^2$.

Subject headings: galaxies: jets — black hole physics — plasmas

1. INTRODUCTION

One of the major problems in astrophysics is the production mechanism of relativistic jets. They are associated with active galactic nuclei (AGNs), Galactic black hole (BH) candidates, and gamma-ray bursts (GRBs). It is inferred that AGN jets have Lorentz factors of $\Gamma \sim 10 - 100$, luminosities as high as the Eddington luminosity L_{Edd} , and opening angles of $\theta_j \sim \Gamma^{-1}$. Although the matter content of AGN jets is still an open problem, the inertia is seemingly dominated by protons (Sikora et al. 2005). The masses of central BHs of AGNs are typically $M \sim 10^7 M_\odot - 10^9 M_\odot$.

An outflow can have a relativistic velocity if the enthalpy per unit rest energy $\mu \equiv L_{j,\text{tot}}/\dot{M}_j c^2 \gg 1$ in the vicinity of the BH, where $L_{j,\text{tot}} = L_B + L_k$ is the total luminosity, L_B and L_k are Poynting and particle kinetic luminosities, respectively, and \dot{M}_j is mass loading rate. If the source of $L_{j,\text{tot}}$ is gravitational energy of the accreting mass on the central BH, we have $L_{j,\text{tot}} < G\dot{M}/R < \dot{M} c^2$, where \dot{M} is mass accretion rate, and radius R should be larger than GM/c^2 . This leads to $\mu/\dot{M}_j \gg 1$, implying that the production mechanism of relativistic jets should be converting gravitational energy into Poynting and/or kinetic energies, and concentrating them on a small fraction of mass.

It is therefore likely that the Poynting and/or kinetic energies are injected in polar region above the rotating BH, ‘the funnel’, where mass loading is exponentially suppressed by the centrifugal barrier (Abramowicz et al. 1978). This configuration is also suitable for the outflow to be collimated by the external pressure. The magnetically dominated jet models, or magnetohydrodynamic (MHD) models, have been recently progressed with numerical simulations (e.g., McKinney 2006). If a certain amount of particles are injected (or generated) in the funnel, the strong poloidal magnetic fields associated with electric currents flowing in the accretion torus accelerate the flow of the particles. The MHD flow can accelerate to a relativistic velocity if suitable boundary conditions are satisfied (Komissarov et al. 2007; Lyubarsky 2009; Granot et al. 2011). On the other hand, the kinetically domi-

nated jet models, so-called fireball models, have been actively discussed for GRB jets, for which the energy injection via $\nu\bar{\nu}$ annihilation could be efficient (Zalamea & Beloborodov 2011). A thermally dominated spherical blob of gas inevitably accelerates to a relativistic velocity (Mészáros et al. 1993; Piran et al. 1993; Kobayashi et al. 1999). It is even possible that large amount of remaining thermal energy at the photosphere is released as prompt γ -ray emission itself (e.g., Toma et al. 2011, and references therein). For AGN jets also, fireball models have been elaborately studied by some authors (e.g., Asano & Takahara 2007, 2009; Becker et al. 2011).

However, the above models do not answer a question ‘‘Why are the Lorentz factors of AGN jets regulated to $\Gamma \sim 10 - 100$? Why not $\Gamma \gg 100$ or $\Gamma \sim$ a few?’’ In either of the MHD or fireball model, mass loading rate into the funnel is essential for determining the final Lorentz factor (and the radiation properties) of jets. There is an interesting idea on this point for GRB jets. Their mass loading might be determined by neutron diffusion from the disk wind surrounding the jet (Levinson & Eichler 2003; McKinney 2005). The jet is considered to have globally ordered magnetic fields that may suppress proton diffusion across the jet-disk wind boundary.¹

In this paper, we discuss the role of the neutrons for mass (as well as energy) injection of AGN jets. We focus on relativistic neutrons escaping from the accretion flow, and calculate the fraction of the total escaping neutrons that decay into protons in the funnel. The processes of the relativistic neutron escape from the BH accretion flow have been discussed by several authors (e.g., Eichler & Wiita 1978; Sikora et al. 1989; Begelman et al. 1990; Atoyan 1992; Contopoulos & Kazanas 1995), although the efficiencies of mass and energy injections in the funnel region have not been studied in detail. In Section 2, we make a short review on proton acceleration and cooling in the accretion flow, and parametrize the spectrum of the escaping neutrons. Then we formulate the geometric injection efficiency in Section 3, and show the results of $L_j/\dot{M} c^2$ and \dot{M}_j/\dot{M} in our model in Sec-

¹ See also Levinson (2006) and Ioka (2010) for other ideas on relativistic jet mass loading.

tion 4. Conclusion and discussion are given in Section 5.

2. RELATIVISTIC NEUTRON PRODUCTION AND ESCAPE

We consider the AGN central engine as follows. A rotating BH has an accretion flow around it. The accretion flow is geometrically thick, and creates a hot corona and/or non-relativistic wind extending vertically, although the polar region above the central BH is dilute because of the centrifugal barrier. There can be large-scale magnetic fields anchored on the accretion flow, which may also suppress protons leaking into the funnel, since the Larmor radius

$$R_L = \frac{\gamma_p m_p c^2}{eB} \simeq 3.1 \times 10^3 \gamma_p B_3^{-1} \text{ cm} \quad (1)$$

is much smaller than the system size characterized by the Schwarzschild radius

$$R_s = \frac{2GM}{c^2} \simeq 3.0 \times 10^{13} M_8 \text{ cm}, \quad (2)$$

where $B_3 = B/(10^3 \text{ G})$ and $M_8 = M/(10^8 M_\odot)$. Neutrons are not affected by the magnetic fields, so that they can be an effective source of mass injection into the funnel.

One may consider the origin of such neutrons as thermal process in the accretion flow. The temperature of protons and heavy nuclei is as high as $kT_p \sim GMm_p/R \sim 500R_*^{-1} \text{ MeV}$, where $R_* \equiv R/R_s$. Then the helium breakup and the pp collisions can produce thermal neutron component. The neutron fraction can be $n_n/(n_n + n_p) \lesssim 0.1$ in the vicinity of the BH (e.g., Filho et al. 2003; Hu & Peng 2008). However, non-relativistic neutrons only survive as long as

$$D \equiv c\tau_n \sim 3 \times 10^{13} \text{ cm}, \quad (3)$$

where $\tau_n \sim 10^3 \text{ s}$ is the decay time of a neutron. This is comparable to the system size characterized by R_s , and thus they cannot reach the funnel in the case of $M \gtrsim 10^8 M_\odot$.

We then focus on relativistic neutrons created in the accretion flow. The plasmas of the geometrically thick AGN accretion flows are generally collisionless for protons (cf. Takahara & Kusunose 1985). In such plasmas, the proton energy distribution is not necessarily Maxwellian, and some fraction of the protons can be accelerated to relativistic speeds. The relativistic hadrons produce relativistic neutron component via the pp and/or $p\gamma$ collisions (Sikora et al. 1989; Begelman et al. 1990). The relativistic neutrons with Lorentz factor γ_n survive over $D\gamma_n \simeq 3 \times 10^{13} \gamma_n \text{ cm}$, so that they can reach the funnel and decay into relativistic protons (and electrons) there. The magnetic coupling in the funnel will isotropize them, leading to the electron-proton fireballs. Neutrons that decay outside the funnel just energize the dense non-relativistic wind.

As for the proton acceleration mechanism in the geometrically thick accretion flows, there are many possibilities, and we do not specify it in this paper. If the accretion results from turbulent viscosity driven by magneto-rotational instability (Balbus & Hawley 1991), the plasma involves magnetic field fluctuations and reconnections, where protons can be accelerated via second-order and/or first-order Fermi processes (e.g., Dermer et al. 1996; Hoshino 2012; Riquelme et al. 2012). The flows may also have regions with strong (less-fluctuated) magnetic fields, where accretion can result from angular momentum transport by magnetically driven winds. Some fields may be oppositely directed, giving rise to magnetic reconnections, which can accelerate particles via first-order Fermi

process (e.g., Drury 2012; de Gouveia Dal Pino et al. 2010; Vieyro & Romero 2012). Furthermore, protons could be accelerated at a standing shock formed in the accretion flow (Becker et al. 2011).

In the following, we make a short review of Sikora et al. (1989) and Begelman et al. (1990) for parametrizing the neutronization factor and the escaping neutron spectrum.

2.1. Spectrum of escaping neutrons

Relevant processes for protons are the accretion inflow, Fermi acceleration, $p\gamma$ cooling, and pp cooling, and those for created neutrons are the escape from the inflow, $n\gamma$ cooling, and np cooling. The proton escape or spatial diffusion is negligible because of the small Larmor radius, whereas protons are advected on the inflow timescale t_{in} :

$$t_{\text{in}} \sim \frac{R}{v_{\text{in}}} = 10 v_{\text{in},-1}^{-1} \frac{R}{c}, \quad (4)$$

where $v_{\text{in}} = 0.1 v_{\text{in},-1} c$ is the accretion fluid velocity. Fermi acceleration timescale is estimated as $t_{\text{acc}} \sim \xi R_L/c \simeq 1.0 \times 10^{-3} \gamma_p \xi_4 B_3^{-1} \text{ s}$, where $\xi = 10^4 \xi_4$ is the factor related to the magnetic field fluctuations. This indicates that the acceleration is so efficient that protons can be highly energized. At high energy ranges, the $p\gamma$ collisions are the most important cooling process, where we assume a typical radiation field with luminosity $10^{-4} L_{\text{Edd}} < L_r < L_{\text{Edd}}$ and spectrum $F_\nu \propto \nu^{-\alpha}$ with $0.5 < \alpha < 1.5$. This assumed radiation field is rather generic, which may include thermal as well as non-thermal emission of electrons. The equality of t_{acc} with the $p\gamma$ cooling timescale $t_{p\gamma}$ leads to the maximum proton Lorentz factor $\gamma_{p,M} \sim 10^7 (B_3 R_*/\xi_4)^{1/2} (L_r/10^{-2} L_{\text{Edd}})^{-1/2}$.

For the BH mass $M \sim 10^7 M_\odot - 10^9 M_\odot$, the system size is $\lesssim 10^{15} \text{ cm}$, so that the protons with $\gamma_p \lesssim 10^2$ (which are converted into neutrons with similar Lorentz factor γ_n) are important. At such energy ranges, the pp collisions are more efficient for creation of neutrons than the $p\gamma$ collisions. The pp cooling time for protons is estimated as

$$t_{pp} \sim \frac{1}{n_p c \sigma_{pp} K_{pp}} \sim 30 \tau_p^{-1} \frac{R}{c}, \quad (5)$$

where n_p and $\tau_p = \sigma_T n_p R$ are the proton number density and the Thomson optical depth at radius R , respectively. The pp cross section is $\sigma_{pp} \sim \sigma_T/17$, and $K_{pp} \simeq 1/2$ is the inelasticity. If $t_{pp} < t_{\text{in}}$, the pp collisions occur efficiently. For $t_{\text{in}} < t_{pp}$, the efficiency reduces by a factor of t_{in}/t_{pp} .

The created neutrons are not magnetically coupled to the background plasma. They escape without being absorbed if $t_{\text{esc}}^{(n)} \sim R/c$ is smaller than the timescales of np and $n\gamma$ collisions, t_{np} and $t_{n\gamma}$, that are similar to t_{pp} and $t_{p\gamma}$, respectively. The maximum Lorentz factor of the escaping neutrons is given by $t_{\text{esc}}^{(n)} = t_{n\gamma}$, as $\gamma_{n,M} \sim 10^6 (L_r/10^{-2} L_{\text{Edd}})^{-1}$.

At lower energy ranges, say $\gamma_p < 10^5$, we have $t_{\text{acc}} < t_{\text{esc}}^{(n)} < \min(t_{\text{in}}, t_{pp}) < \max(t_{\text{in}}, t_{pp}) < t_{p\gamma}$, for $\tau_p < 20$. In this case, neutrons created by pp collisions freely escape from the accretion flow. The kinetic equations for the proton and neutron number densities in the steady state and for a power-law proton injection function $\dot{N}_p \propto \gamma_p^{-p}$ indicate that the ratio of the escaping neutron number flux \dot{N}_n to the proton injection flux is estimated as

$$f_n \equiv \frac{\dot{N}_n}{\dot{N}_p} \sim \frac{1}{2(p-1)+1} \min\left(1, \frac{t_{\text{in}}}{t_{pp}}\right). \quad (6)$$

The numerical factor 2 in the denominator is determined by the probability of the charge exchange during a single pp collision and K_{pp} . The neutron spectrum is given by $\dot{N}_n \propto \gamma_n^{-p}$ for the low-energy range satisfying $t_{pp} < t_{p\gamma}$. It deviates from a single power-law at high energy, say $\gamma_n > 10^5$ (see Fig. 7 of Begelman et al. 1990), although the neutrons at such high energy ranges are not relevant for our purpose in this paper.

The process of the creation and escape of neutrons with $\gamma_n < 10^5$ is most effective for $t_{\text{esc}}^{(n)} < t_{np}$ and $t_{pp} < t_{\text{in}}$, i.e.,

$$3v_{\text{in},-1} < \tau_p < 20, \quad (7)$$

for which we have $f_n \sim 1/[2(p-1)+1]$. It may be possible that geometrically thick accretion flows satisfy this condition of τ_p . To confirm it in detail, however, modeling of accretion flows with significant neutron energy release is required, which we leave as separate work.

3. CALCULATION OF THE GEOMETRIC EFFICIENCY

The luminosity of the escaping neutrons is parametrized by $L_n = f_n f_a f_{\text{th}} \dot{M} c^2$, where f_{th} is the ratio of the heating rate of protons to $\dot{M} c^2$, f_a is the ratio of the rate for accelerated protons to the heating rate of protons, and f_n is the neutronization factor estimated by Eq. (6). The heating rate can be as high as $\sim (1/2)GMM/R_s \sim Mc^2/4$, i.e., $f_{\text{th}} \lesssim 0.3$, while we have $f_n \lesssim 1/[2(p-1)+1] \lesssim 0.3$ for a reasonable range $p > 2$. It is difficult to estimate the acceleration fraction f_a . We only have a rough constraint $f_a \lesssim 0.3$, which means that the energy density of the accelerated protons will not dominate that of thermal protons. Therefore we may summarize the microphysical efficiency as

$$f_n f_a f_{\text{th}} \lesssim 3 \times 10^{-2}. \quad (8)$$

The neutrons with this luminosity are released isotropically, and the protons created via the neutron decays are magnetically coupled and energize the background plasma. Here we calculate the geometric efficiency, i.e., the fraction of neutrons that decay into protons at the polar region. In order to obtain the order of magnitude of the geometric efficiency, we set a simple configuration of the BH accretion system, and calculations are performed by assuming the Euclidean space.

As illustrated in Figure 1, we consider an accretion torus with $H/R = 1/\tan\theta_0$ around a BH, which is located at the center of the coordinate system. The neutron emission region is assumed as the inner fraction of this torus between the cylindrical radii $\rho_m = R_s$ and $\rho_M = 3R_s$. We assume that the neutron emissivity is uniform in this region for simplicity. The spatial volume of this region is $V = (4/3)\pi(\rho_M^3 - \rho_m^3)/\tan\theta_0$. Then the neutron emissivity is given by $dE^{(n)}/dt dV d\Omega d\gamma \equiv j_\gamma^{(n)} = A\gamma^{-p+1}$ for $1 \leq \gamma \leq \gamma_M$, where $A = L_n/(4\pi V \int_1^{\gamma_M} \gamma^{-p+1} d\gamma)$. Hereafter we will not distinguish the Lorentz factors of protons and neutrons, since the neutrons with γ_n decay into protons with $\gamma_p \sim \gamma_n$. The dilute polar region is set as the cone with the opening angle θ_1 . We assume that $\theta_1 \sim O(1)$ for $r_1 = R_s < r_j < r_2$, and consider that r_2 is a characteristic radius above which the collimation becomes strong due to the pressure from the hot corona and/or disk wind. The collimation suppresses the energy injection for $r_j > r_2$. We will take $r_2 = 10R_s$ as a fiducial case below.

Let us consider a straight line with a parameter s crossing the surfaces of the emission region at $s = s_1$ and $s = s_2$. The fractional neutron intensity emitted from the line element $\Delta\bar{s}$ at $s_1 < \bar{s} < s_2$ and measured at a point s in the

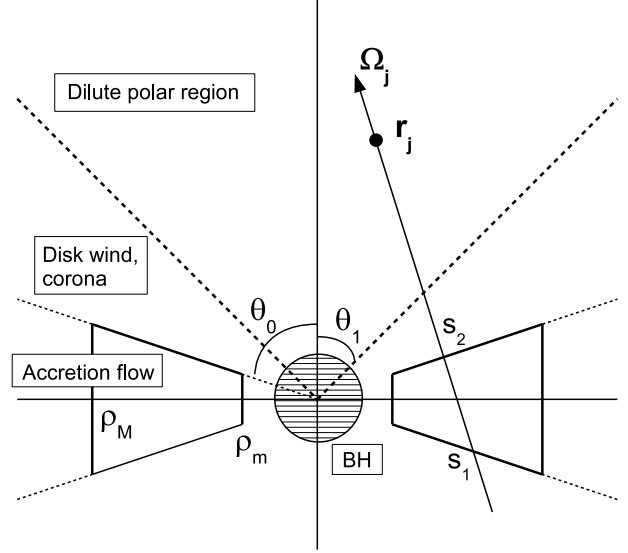


FIG. 1.— Structure of the BH accretion system for the calculation of the geometric efficiency. The BH is at the center of the coordinate system. The accretion flow with thickness $H/R = 1/\tan\theta_0$ has the neutron emission region between the cylindrical radii $\rho_m = R_s$ and $\rho_M = 3R_s$. A trajectory of neutrons incident to the point $\mathbf{r}_j = (r_j, \theta_j, \varphi_j)$ is shown. The dilute polar region is assumed to be a cone with the opening angle θ_1 for $r_j < r_2 = 10R_s$, and strongly collimated for $r_j > r_2$.

polar region is $\Delta I_\gamma^{(n)}(s) = j_\gamma^{(n)}(\bar{s})\Delta\bar{s}$, if neutron decay is not taken into account. We may approximate the proton intensity created at $s_j < s < s_j + ds_j$ through the neutron decay as $\partial\Delta I_\gamma^{(p)}/\partial s_j = \Delta I_\gamma^{(n)}(s)\delta(s_j - \bar{s} - D\gamma)$. Integrating this over $s_1 < \bar{s} < s_2$, we obtain the proton emissivity created at s_j from the neutrons propagating through a single line as

$$\begin{aligned} j_\gamma^{(p)}(s_j) &\equiv \frac{\partial I_\gamma^{(p)}}{\partial s_j}(s_j) = \int_{s_1}^{s_2} j_\gamma^{(n)}(\bar{s})\delta(s_j - \bar{s} - D\gamma)d\bar{s} \\ &= \begin{cases} A\gamma^{-p+1} & (s_j - s_2 < D\gamma < s_j - s_1), \\ 0 & (\text{otherwise}) \end{cases} \end{aligned} \quad (9)$$

For a given point $\mathbf{r} = \mathbf{r}_j$ (corresponding to s_j), s_1 and s_2 are functions of the incident direction, i.e., $s_1 = s_1(\Omega_j)$ and $s_2 = s_2(\Omega_j)$. We obtain the energy injection rate of protons per unit volume at a point $\mathbf{r} = \mathbf{r}_j$ by integrating $j_\gamma^{(p)}(s_j)$ over solid angle, $dE^{(p)}/dt dV_j d\gamma \equiv \dot{u}_\gamma^{(p)}(\mathbf{r}_j) = \int d\Omega_j j_\gamma^{(p)}(s_j)$. This leads to the mass injection rate per unit volume as $dM^{(p)}/dt dV_j d\gamma = \dot{u}_\gamma^{(p)}(\mathbf{r}_j)/(\gamma c^2)$. Finally we obtain the total energy and mass injection rates by integrating $\dot{u}_\gamma^{(p)}$ and $\dot{u}_\gamma^{(p)}/(\gamma c^2)$, respectively, over the total energy range and the volume of the polar region. The efficiencies of the neutron energy and mass injections are thus written by

$$\left\{ \frac{L_j/(\dot{M}c^2)}{M_j/\dot{M}} \right\} = \frac{2\pi}{\dot{M}c^2} \int_0^{\theta_1} d\theta_j \sin\theta_j \int_{R_s}^{r_2} dr_j r_j^2 \times \int_1^{\gamma_M} d\gamma \int d\Omega_j \left\{ \frac{j_\gamma^{(p)}}{j_\gamma^{(p)}/\gamma} \right\}, \quad (10)$$

where the axisymmetry of this system has allowed us to perform the integration over the azimuthal angle φ_j , and we set the upper bound of the r_j integration as r_2 since the energy injection is assumed to be much less effective for $r_j > r_2$ due to strong collimation. The free parameters for calculating the efficiencies for a given BH mass M are $\tan\theta_0, p, \gamma_M, r_2, \tan\theta_1$,

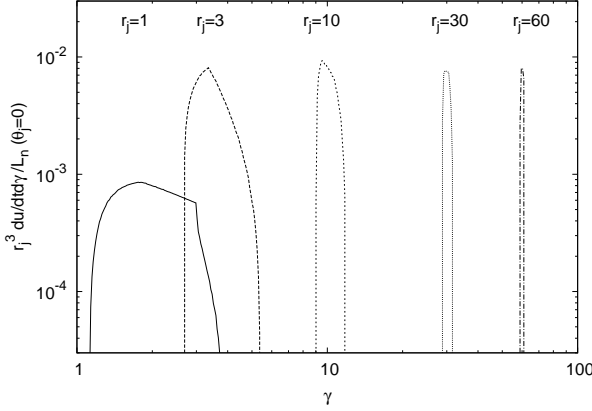


FIG. 2.— Fraction of spectral energy injection rate per unit volume $u_\gamma^{(p)}(\mathbf{r}_j)$ (times r_j^3) of protons at the pole ($\theta_j = 0$) of various radii r_j , with respect to the escaping neutron luminosity $L_n = f_n f_a f_{\text{th}} \dot{M} c^2$, for the case of $M_8 = 1$. The lines from left to right correspond to $r_j = 1, 3, 10, 30$, and 60 , respectively (measured in unit of D). The other parameters are $\tan \theta_0 = 2, p = 2$, and $\gamma_M = 10^2$.

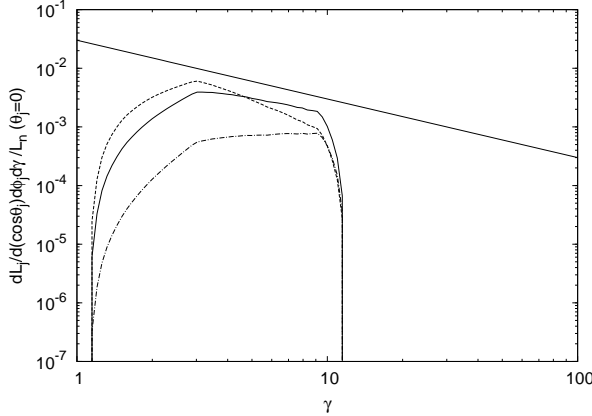


FIG. 3.— Fraction of spectral energy injection rate per unit solid angle for $1 < r_j < r_2 = 10$ $dL_j/d(\cos \theta_j)d\varphi_j d\gamma = \int_{\tilde{r}_1}^{r_2} dr_j r_j^2 u_\gamma^{(p)}$ at the pole ($\theta_j = 0$), with respect to $L_n = f_n f_a f_{\text{th}} \dot{M} c^2$, for the case of $M_8 = 1$ with $\tan \theta_0 = 2$ and $\gamma_M = 10^2$. The solid, dashed, and dot-dashed lines correspond to the cases of $p = 2, p = 3$, and $p = 1$, respectively. For reference, we plot a power-law function $\propto \gamma^{-1}$ by the solid straight line.

and $f_n f_a f_{\text{th}}$.

4. RESULTS

4.1. Case of $M = 10^8 M_\odot$

Here we show the calculation results for the case of $M_8 = 1$. In this section we measure lengths in unit of D . Since R_s happens to be equal to D in this case, we have $\rho_m = 1$ and $\rho_M = 3$. The other parameters are set to be $\tan \theta_0 = 2, p = 2, \gamma_M = 10^2, r_2 = 10$, and $\tan \theta_1 = 1$. We will examine the dependence of results on these parameters later. First, we show the integration result of $u_\gamma^{(p)}(\mathbf{r}_j) = \int d\Omega_j j_\gamma^{(p)}(s_j)$ to see the spectral property of the injection rate at various points. We plot $r_j^3 u_\gamma^{(p)}/L_n$ at the pole $\theta_j = 0$ of various radii $r_j = 1, 3, 10, 30$, and 60 in Figure 2. We can see that the injected protons are distributed over relatively broad energy range at $r_j \lesssim 3$, while concentrated to $\gamma \sim r_j$ at large radii $r_j \gtrsim 3$. This indicates that for large r_j , neutrons decay after traversing large distances, so that the detailed structure of the emission region is not relevant.

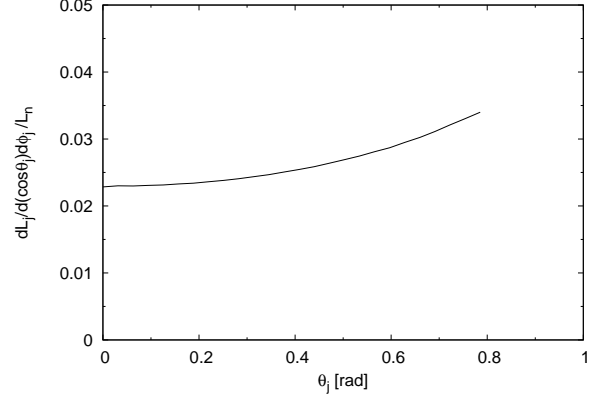


FIG. 4.— Fraction of energy injection rate per unit solid angle for $1 < r_j < r_2 = 10$ ($dL_j/d(\cos \theta_j)d\varphi_j = \int_1^{\gamma_M} d\gamma \int_{\tilde{r}_1}^{r_2} dr_j r_j^2 u_\gamma^{(p)}$) with respect to $L_n = f_n f_a f_{\text{th}} \dot{M} c^2$ as a function of θ_j for the case of $M_8 = 1$ with the other parameters $\tan \theta_0 = 2, p = 2$, and $\gamma_M = 10^2$.

Next we show the integration result of $\int_{\tilde{r}_1}^{r_2} dr_j r_j^2 u_\gamma^{(p)}$ at the pole, which is equivalent to $dL_j/d(\cos \theta_j)d\varphi_j d\gamma$. We plot this value, normalized by L_n , in Figure 3. We also show the results for $p = 1$ and $p = 3$. For $p = 2$, comparing the result with the injection power-law profile $\propto \gamma^{-p+1}$, we find that the energy is injected efficiently for $\gamma \sim 3 - 10$, and has the similar spectrum as the injected one. This property is explained simply as follows. At the large radii, say $r_j > \tilde{r}_1$, where the detailed structure of the emission region is not relevant, the solid angles of the incident neutron directions are limited within a small range $\Delta\Omega_j \sim S/r_j^2$, where S is the horizontal cross section of the emission region. Also we may write $j_\gamma^{(p)}(r_j) = j_\gamma^{(n)} \delta(r_j - \gamma)h$, where h represents the mean width of the emission region. Note that we measure r_j in unit of D . These approximations lead to

$$\begin{aligned} \frac{1}{L_n} \int_{\tilde{r}_1}^{r_2} dr_j r_j^2 u_\gamma^{(p)} &\sim \frac{1}{4\pi V \int_1^{\gamma_M} \gamma^{-p+1} d\gamma} \times \\ &\int_{\tilde{r}_1}^{r_2} dr_j r_j^2 \int d\Omega_j \gamma^{-p+1} \delta(r_j - \gamma)h \\ &\sim \begin{cases} \frac{1}{4\pi \int_1^{\gamma_M} \gamma^{-p+1} d\gamma} \gamma^{-p+1} & (\tilde{r}_1 < \gamma < r_2) \\ 0 & (\text{otherwise}), \end{cases} \end{aligned} \quad (11)$$

where we set $Sh \sim V$. Since we have $1/(4\pi \int_1^{\gamma_M} \gamma^{-p+1} d\gamma) = 0.017$ for $p = 2$ and $\gamma_M = 10^2$, this rough calculation well agrees with the numerical integration for $3 \lesssim \gamma \lesssim 10$. For $\gamma < 3$, the spatial volume of emitting points that can connect to the pole with decay lengths of $\sim \gamma$ is smaller, so that the injected energy is smaller.

We integrate $\frac{1}{L_n} \int_{\tilde{r}_1}^{r_2} dr_j r_j^2 u_\gamma^{(p)}$ over $1 < \gamma < \gamma_M = 10^2$ and then obtain $\frac{1}{L_n} dL_j/d(\cos \theta_j)d\varphi_j = 0.023$ at $\theta_j = 0$. We also show the calculation results of $\frac{1}{L_n} dL_j/d(\cos \theta_j)d\varphi_j$ as a function of θ_j in Figure 4. This shows that the energy injection rate does not strongly depend on θ_j . The slight increase for larger θ_j is due to larger contribution for the energy range $\gamma < 3$, but this contribution is confirmed to be not significant for the total energy injection L_j in the case of $\tan \theta_1 = 1$.

Finally we integrate $\frac{1}{L_n} dL_j/d(\cos \theta_j)d\varphi_j$ over $0 < \theta_j < \theta_1 = \pi/4$ and multiplied by 2π , obtaining $L_j/L_n = 0.051$. This provides the total energy injection efficiency for the param-

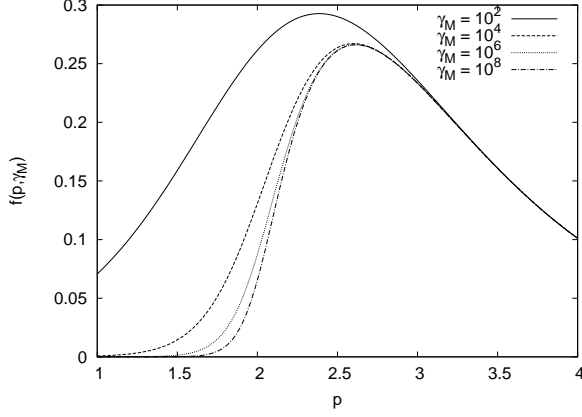


FIG. 5.— Factor $\int_3^{10} \gamma^{-p+1} d\gamma / \int_1^{\gamma_M} \gamma^{-p+1} d\gamma$ is plotted as a function of p for various γ_M .

eter values $\tan\theta_0 = 2$, $p = 2$, $\gamma_M = 10^2$, $r_2 = 10$, $\tan\theta_1 = 1$ as $L_j/(\dot{M}c^2) = 0.051 f_n f_a f_{th}$.

The geometric efficiency is roughly estimated by integrating Eq. (11) with $d(\cos\theta_j)d\varphi_j d\gamma$,

$$\frac{L_j}{L_n} \sim \frac{2\pi(1-\cos\theta_1)}{4\pi} \frac{\int_{\tilde{r}_1}^{r_2} \gamma^{-p+1} d\gamma}{\int_1^{\gamma_M} \gamma^{-p+1} d\gamma}, \quad (12)$$

which gives $\simeq 0.04$, if $\tilde{r}_1 = 3$ is taken. The slight difference between this rough estimate and the numerical calculation comes from treating the energy injection rate as constant over θ_j and neglecting the contribution for $\gamma < 3$. The above rough estimate is useful, which simply consists of the two factors, the ratio of the solid angle of the polar region to 4π and the ratio of the energy in the effective injection range $\tilde{r}_1 < \gamma < r_2$ to the total range $1 < \gamma < \gamma_M$.

We confirm that the difference of the torus thickness $\tan\theta_0$ does not substantially change the value of the geometric efficiency. This is attributed to the fact that the energy injection is effective for large radii, for which the structure of the emission region is not relevant. The differences of the other parameter values, p , γ_M , r_2 , and $\tan\theta_1$, affect the efficiency according to the simple formula Eq. (12).

In fact, γ_M is typically much larger than 10^2 (see Section 2.1), which may significantly reduce the efficiency. To check this, we plot the factor $\int_{\tilde{r}_1}^{r_2} \gamma^{-p+1} d\gamma / \int_1^{\gamma_M} \gamma^{-p+1} d\gamma$ in Eq. (12) for $\tilde{r}_1 = 3$, $r_2 = 10$, and various γ_M in Figure 5. It is found that this factor for $\gamma_M > 10^4$ still can have a high value ~ 0.25 when the power-law index is $p \sim 2.3-3$. For $\gamma_M = 10^6$ and $p = 2.5$, the result of the numerical integration is

$$\frac{L_j}{\dot{M}c^2} = 0.059 f_n f_a f_{th}, \quad (13)$$

while the approximate estimate gives us $L_j/(\dot{M}c^2 f_n f_a f_{th}) \sim 0.04$. Note that this corresponds to the maximum level of the efficiency in this system, which is obtained for the parameters $p = 2.3-3$, $\tan\theta_1 = 1$, and $r_2 = 10$. However, we consider that such parameter values are within realistic ranges.

The numerical calculation gives us the mass injection efficiency for $\gamma_M = 10^6$ and $p = 2.5$

$$\frac{\dot{M}_j}{\dot{M}} = 0.019 f_n f_a f_{th}. \quad (14)$$

This indicates that the injected protons will be isotropized and

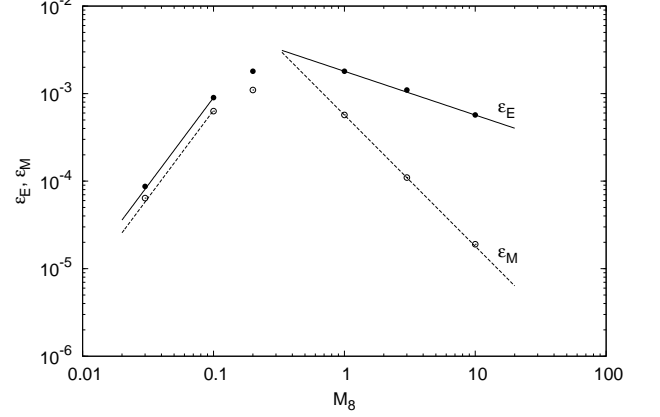


FIG. 6.— Results of the calculations of the energy injection efficiency $\epsilon_E = L_j/\dot{M}c^2$ (filled circles) and of the mass injection efficiency $\epsilon_M = \dot{M}_j/\dot{M}$ (open circles) as a function of $M_8 = M/(10^8 M_\odot)$ with the parameters $f_n f_a f_{th} = 3 \times 10^{-2}$, $\tan\theta_0 = 2$, $p = 2.5$, $\gamma_M = 10^6$, $r_2 = 10R_s$, and $\tan\theta_1 = 1$. For $M_8 \gtrsim 0.3$, $\epsilon_E \propto M_8^{p+2}$ (represented by solid line) and $\epsilon_M \propto M_8^{p+1}$ (dashed line), consistent with the approximate formula Eq. (12), while for $M_8 \leq 0.1$, ϵ_E and ϵ_M both $\propto M_8^2$ (solid and dashed lines), consistent with the approximate formula Eq. (15). The final Lorentz factor of the jet (without an additional energy input) is given by $\Gamma = \epsilon_E/\epsilon_M$.

have mean random Lorentz factor $\langle\gamma\rangle = L_j/(\dot{M}_j c^2) = 3.1$. If no additional energy is injected into the polar region, the fireball model predicts that the random kinetic energy is transferred to the bulk kinetic energy with terminal Lorentz factor $\Gamma \simeq 3.1$.

4.2. Dependence on BH mass

We also perform calculations for various values of BH mass. For the case of $M_8 = 10$, the neutron emission region is set between $\rho_m = 10$ and $\rho_M = 30$. We find that many of the properties for this case are just a scale-up version of those for $M_8 = 1$ discussed above. The energy is injected mainly for $\gamma \sim 30-100$ in the case of $r_2 = 100$. The energy injection efficiency is approximately estimated by Eq. (12). For $p > 2$, the energy in the range $\gamma \sim 30-100$ is smaller than that in $\gamma \sim 3-10$, so that we have smaller energy injection in this case. Since the mean Lorentz factor of the injected protons $\langle\gamma\rangle$ is larger, the mass injection efficiency is even smaller.

We plot the calculated $L_j/(\dot{M}c^2)$ and \dot{M}_j/\dot{M} for $M_8 = 3$ and 10 with the same parameters as for Eqs. (13) and (14) and $f_n f_a f_{th} = 3 \times 10^{-2}$ in Figure 6. The approximate formula Eq. (12) implies that $L_j/\dot{M}c^2 \propto r_2^{p+2} \propto M_8^{p+2}$ for given θ_1 and γ_M , which agrees with the numerical results. The mean Lorentz factor should linearly depend on the length scale, i.e., $\langle\gamma\rangle \propto M_8$, leading to $\dot{M}_j/\dot{M} = L_j/(\langle\gamma\rangle \dot{M}c^2) \propto M_8^{-p+1}$, which also agrees with the numerical results. These scalings are applicable for cases of $\tilde{r}_1 > 1$, i.e., $M_8 \gtrsim 0.3$.

For the case of $M_8 = 0.1$, the system size is smaller than the case of $M_8 = 1$, i.e., $\rho_m = 0.1$, $\rho_M = 0.3$, and $r_2 = 1$. In this case most of the energy is injected into a region at $r_j > r_2$, which is assumed to be significantly collimated, so that the injection efficiency should be smaller than the case of $M_8 = 1$. Let us assume that the dilute polar region is cylindrical at $r_j > r_2$ for simplicity, and then integrate $u_\gamma^{(p)}$ and $u_\gamma^{(p)}/(\gamma c^2)$ for the energy and mass injection, respectively, over $1 < \gamma < \gamma_M$ and the volume of the polar region at $r_j \geq 1$ to deduce the efficiencies. The results (and those for the cases of $M_8 = 0.03$ and 0.2) are plotted in Figure 6.

We can also derive an approximate formula of the energy

injection efficiency for $M_8 \leq 0.1$. In the cylindrical region, we have the opening angle as a function of r_j as $\theta_c \simeq \theta_1 r_2 / r_j$. The geometric efficiency may be estimated as

$$\begin{aligned} \frac{L_j}{f_n f_a f_{\text{th}} \dot{M} c^2} &\sim \frac{1}{2V \int_1^{\gamma_M} \gamma^{-p+1} d\gamma} \\ &\times \int_1^\infty d\gamma \int_1^\infty dr_j r_j^2 \left(\frac{\theta_c^2}{2} \right) \int d\Omega_j \gamma^{-p+1} \delta(r_j - \gamma) h \\ &\sim \frac{\theta_1^2 r_2^2}{4} \frac{\int_1^\infty \gamma^{-p-1} d\gamma}{\int_1^{\gamma_M} \gamma^{-p+1} d\gamma} \simeq 0.03 r_2^2, \quad (r_2 \leq 1) \end{aligned} \quad (15)$$

where the final results are obtained for $p = 2.5$, $\gamma_M = 10^6$, and $\tan \theta_1 = 1$. For $p \sim 2.3 - 3$ and $\gamma_M > 10^4$, the efficiency ranges between $0.02 r_2^2$ and $0.05 r_2^2$. This equation clearly indicates that the energy injection is smaller for smaller $M_8 (= 0.1 r_2)$ in the case of $r_2 \leq 1$. The mean Lorentz factor may be estimated as $\langle \gamma \rangle = \int_1^\infty \gamma^{-p-1} d\gamma / \int_1^\infty \gamma^{-p-2} d\gamma \approx (p+1)/p$. Those approximate formulae agree with the numerical results of $L_j / \dot{M} c^2$ and \dot{M}_j / \dot{M} .

5. CONCLUSION AND DISCUSSION

The luminosity of the relativistic neutrons from geometrically thick AGN accretion flow is estimated as $L_n = f_n f_a f_{\text{th}} \dot{M} c^2$, and $f_n f_a f_{\text{th}}$ can be as high as $\sim 3 \times 10^{-2}$, where the thermalization fraction of the accretion power $f_{\text{th}} \lesssim 0.3$, the energy fraction of the accelerated protons in the thermal energy $f_a \lesssim 0.3$, and the neutronization (and escape) fraction $f_n \lesssim 0.3$. Those neutrons escape isotropically, a fraction of which decay into protons at the dilute polar region and inject the energy and mass into the relativistic jet. We have calculated this geometric fraction by setting a simple system consisting of the central BH, the accretion flow including the neutron emission region (at $R_s \leq \rho \leq 3R_s$), and the polar region. The polar region is assumed to be a cone with an opening angle of $\theta_1 \sim O(1)$ at $r_1 = R_s < r_j < r_2 = 10R_s$ and changed to be a cylinder, at $r_j > r_2$ as a rough approximation of the significant collimation.

The results are plotted in Figure 6, for which the parameters are chosen as $\tan \theta_0 = 2$, $r_2 = 10R_s$, $\tan \theta_1 = 1$, $p = 2.5$, $\gamma_M = 10^6$, and $f_n f_a f_{\text{th}} = 3 \times 10^{-2}$, and they are well approximated by Eqs. (12) for $M_8 \gtrsim 0.3$ and (15) for $M_8 \leq 0.1$. The efficiencies $L_j / \dot{M} c^2$ and \dot{M}_j / \dot{M} do not significantly depend on the torus thickness characterized by $\tan \theta_0$, because the energy injection is effective for large radii, for which the structure of the emission region is not relevant. The efficiencies are larger for the larger polar region, i.e., larger r_2 and/or θ_1 , according to Eqs. (12) and (15). They are also weak functions of p and γ_M for $2.3 < p < 3$ and $\gamma_M > 10^4$, which are considered to be realistic ranges.

For $M \sim 10^8 M_\odot$, this process can produce a relativistic jet with $L_j \sim 2 \times 10^{-3} \dot{M} c^2$ and $\dot{M}_j \sim 6 \times 10^{-4} \dot{M}$, leading

to the final Lorentz factor $\Gamma \sim 3$ (if no other types of energies are injected). Most of the relativistic neutron luminosity $L_n \sim 3 \times 10^{-2} \dot{M} c^2$ is injected outside the polar region, which may contribute to the dense non-relativistic disk wind energy. The existence of such energetic disk winds is not incompatible with observations (Tombesi et al. 2011, 2012). The main part of the accretion power $\dot{M} c^2$ is carried by protons and magnetic fields, which may also contribute to the relativistic jet and the non-relativistic disk wind, or just be swallowed by the central BH.

The observations suggest that the luminosities of AGN jets are broadly distributed over $L_{j,\text{tot}} \lesssim \dot{M} c^2$ (e.g., Fernandes et al. 2011; Punsly & Zhang 2011; Ghisellini et al. 2010). Our results imply that jets with $L_{j,\text{tot}} \lesssim 2 \times 10^{-3} \dot{M} c^2$ may be produced by the neutron decay process by itself. In this model, larger BH masses are associated with larger final Lorentz factors of the jets for $M > 10^8 M_\odot$.

For AGN jets with higher luminosities, the neutron decays still can be a dominant mass loading process, whereas they can have additional energy inputs, such as Poynting flux. The mass loading $\dot{M}_j \sim 6 \times 10^{-4} \dot{M}$ leads to e.g., $\Gamma \sim 50$ for $L_{j,\text{tot}} \sim 3 \times 10^{-2} \dot{M} c^2$. If the additional energy input scales as $L_{j,\text{tot}} \propto M$, jets with larger Γ are associated with smaller M for $M < 10^8 M_\odot$ and with larger M for $M > 10^8 M_\odot$.

We have simplified the configuration of the BH accretion system, approximated the amount of the created protons as a delta function of the traversing distance of neutrons (Eq. 9), and assumed the Euclidean space, to obtain orders of magnitudes of the geometric efficiencies. This study has provided the useful approximate formulae Eqs. (12) and (15). More sophisticated formulations and calculations, taking into account the collimating shape of the dilute polar region, radial dependence of the neutron emissivity, detailed process of the neutron decay, and geometry around the Kerr BH, are worth investigating in separate papers.

While we have focused on the geometrically thick disks in this paper, the proton acceleration and the relativistic neutron production may be effective also in hot coronae above the geometrically thin disks (e.g., Drury 2012; de Gouveia Dal Pino et al. 2010; Vieyro & Romero 2012). Similar scalings of the energy and mass injections to the outflows are expected. In any cases, it is important to discuss the mechanism for regulating $\Gamma \sim 10 - 100$ of AGN jets and the role of the neutron component.

We thank the referee for useful comments. K.T. thanks M. Sikora and A. Janiuk for useful discussions and Nicolaus Copernicus Astronomical Center for the hospitality during his stay. This work is partly supported by JSPS Research Fellowships for Young Scientists No. 231446 (K.T.) and by KAKENHI 20540231 (F.T.).

REFERENCES

- Abramowicz, M., Jaroszynski, M., & Sikora, M. 1978, *A&A*, 63, 221
 Asano, K., & Takahara, F. 2007, *ApJ*, 655, 762
 Asano, K., & Takahara, F. 2009, *ApJ*, 690, L81
 Atoyán, A. M. 1992, *A&A*, 257, 465
 Balbus, S. A., & Hawley, J. F. 1991, *ApJ*, 376, 214
 Becker, P. A., Das, S., & Le, T. 2011, *ApJ*, 743, 47
 Begelman, M. C., Rudak, B., & Sikora, M. 1990, *ApJ*, 362, 38
 Contopoulos, J., & Kazanas, D. 1995, *ApJ*, 441, 521
 de Gouveia Dal Pino, E. M., Piovezan, P. P., & Kadowaki, L. H. S. 2010, *A&A*, 518, 5
 Dermer, C., Miller, J. A., & Li, H. 1996, *ApJ*, 456, 106
 Drury, L. O. 2012, *MNRAS*, 422, 2474
 Eichler, D., & Witta, P. J. 1978, *Nature*, 274, 38
 Fernandes, C. A. C., et al. 2011, *MNRAS*, 411, 1909
 Filho, C. M., Lima, C. L., Miyake, H., & Timoteo, V. 2003, *ApJ*, 595, 322
 Ghisellini, G., et al. 2010, *MNRAS*, 402, 497
 Granot, J., Komisarov, S. S., & Spitkovsky, A. 2011, *MNRAS*, 411, 1323

- Hoshino, M. 2012, PRL, 108, 5003
Hu, T., & Peng, Q. 2008, ApJ, 681, 96
Ioka, K. 2010, Prog. Theo. Phys., 124, 667
Kobayashi, S., Piran, T., & Sari, R. 1999, ApJ, 513, 669
Komissarov, S. S., Barkov, M. V., Vlahakis, N., & Königl, A. 2007, MNRAS, 380, 51
Levinson, A. 2006, ApJ, 648, 510
Levinson, A., & Eichler, D. 2003, ApJ, 594, L19
Lyubarsky, Y. 2009, ApJ, 698, 1570
McKinney, J. C. arXiv:astro-ph/0506368
McKinney, J. C. 2006, MNRAS, 368, 1561
Meirelles, C., Lima, C. L., Miyake, H., & Timoteo, V. 2003, ApJ, 595, 322
Mészáros, P., Laguna, P., & Rees, M. J. 1993, ApJ, 415, 181
Piran, T., Shemi, A., & Narayan, R. 1993, MNRAS, 263, 861
Punsly, B., & Zhang, S. 2011, ApJ, 735, L3
Riquelme, M. A., Quataert, E., Sharma, P., & Spitkovsky, A. 2012, submitted (arXiv:1201.6407)
Sikora, M., Begelman, M. C., Madejski, G. M., & Lasota, J.-P. 2005, ApJ, 625, 72
Sikora, M., Begelman, M. C., & Rudak, B. 1989, ApJ, 341, L33
Takahara, F., & Kusunose, M. 1985, Prog. Theo. Phys., 73, 1390
Toma, K., Wu, X.-F., & Mészáros, P. 2011, MNRAS, 415, 1663
Tombesi, F., Sambruna, R. M., Reeves, J. N., Reynolds, C. S., & Braitto, V. 2011, MNRAS, 418, L89
Tombesi, F., Cappi, M., Reeves, J. N., & Braitto, V. 2012, MNRAS, 422, L1
Vieyro, F. L., & Romero, G. E. 2012, A&A, 542, 7
Zalamea, I., & Beloborodov, A. M. 2011, MNRAS, 410, 2302